Reaction Product Imaging: The H + D_2 Reaction

Theofanis N. Kitsopoulos, Mark A. Buntine, David P. Baldwin, Richard N. Zare, David W. Chandler*

The differential cross section for the H + D_2 → HD + D reaction has been measured using a technique called reaction product imaging. In this experiment, a photolytically produced beam of hydrogen (H) atoms crossed a beam of cold deuterium (D_2) molecules. Product D atoms were ionized at the intersection of the two particle beams and accelerated toward a position-sensitive detector. The ion images appearing on the detector are two-dimensional projections of the three-dimensional velocity distribution of the D atom products. The reaction was studied at nominal center-of-mass collision energies of 0.54 and 1.29 electron volts. At the lower collision energy, the measured differential cross section for D atom production, summed over all final states of the HD(*v*,*J*) product, is in good agreement with recent quasi-classical trajectory calculations. At the higher collision energy, the agreement between the theoretical predictions and experimental results is less favorable.

Reaction dynamics can be said to have emerged as a separate branch of chemistry in 1929 with the publication by London (*1*) of the quantum mechanical expression for the potential energy of the hypothetical reaction A + B–C → A–B + C. Two years later, Eyring and Polanyi (*2*) published the first attempt to map out the potential energy surface for the hydrogen exchange reaction, H + H_2. Since then, a tremendous amount of theoretical and experimental effort has been directed toward determining the detailed nature of bimolecular interactions.

The study of bimolecular reactions under single-collision conditions has dramatically improved our understanding of chemical reactivity. Measurements of the nascent product internal state distributions (integral cross sections) and the product velocity distributions (differential cross sections) have led to a fundamental understanding of how chemical reactions proceed. Information concerning the size and position of energetic barriers, the geometry and lifetime of the reaction complex, and product branching ratios and energy partitioning can now be obtained from these measurements. This information is needed for adequately testing the theoretical potential energy surfaces for chemical reactions and the scattering calculations carried out with them.

In our laboratory, we have implemented an ion-imaging technique for studying the differential cross section of a neutral bimolecular reaction. Beginning in 1987 (*3*), ion-imaging techniques have been used for the measurement of photofragment velocity distributions (speed and angle) from unimolecular dissociation processes. Those experiments demonstrated the power of the technique in several ways. First, if the experiment is designed such that the symmetry axis of the velocity distribution is oriented parallel to the face of the imaging detector, one image is all that is required to define uniquely the three-dimensional (3-D) angular distribution. Second, the multiplexing advantage of measuring all angles at once reduces the time necessary to determine a velocity distribution. Third, the technique offers two modes of operation. One mode involves imaging of the atomic fragment or reaction product, which results in measurements that are characterized by moderate energy resolution, comparable to that of conventional time-of-flight (TOF) experiments, in which the internal energy distribution of the products is determined by measuring their kinetic energies. Ion images of atomic products are extremely useful in providing the overall appearance of the differential cross section for a reaction or photofragmentation process because they contain information concerning all product channels. The alternative mode relies on imaging of the molecular fragment or reaction product in a quantum state–selective manner, thus enabling differential cross section measurements for a single rotational-vibrational (rovibronic) state of the molecular product. We report here preliminary measurements of the differential cross section (DCS) for the H + D_2 → HD + D reaction in which the D atom product is imaged. The reaction is studied at relative collision energies of 0.54 and 1.29 eV, and we compare our results to theoretical quasi-classical trajectory (QCT) calculations of Aoiz *et al.* (*4*), which are based on the LSTH (Liu-Siegbahn-Truhlar-Horowitz) (*5*) potential energy surface.

The H + H_2 exchange reaction (and its isotopic variants) is the simplest bimolecular chemical reaction, yet experimental characterization comparable to the level of the calculations has been possible only in the last 7 years. Two types of experimental efforts can be identified: those that determine the integral cross sections for the reaction and those that measure DCSs. Almost simultaneously, rotationally resolved state-to-state integral cross sections were measured by Zare and co-workers (*6*), using resonance-enhanced multiphoton ionization (REMPI), and by Valentini and co-workers (*7*), using coherent anti-Stokes Raman spectroscopy. The reactions studied were H+ *para*-H_2, H + D_2, and D + H_2 at energies between 0.5 and 2.2 eV. Overall, the results of these experiments agree fairly well with theoretical predictions (*8*–*12*).

The DCS measurements that have been made were possible only through the use of crossed-beam TOF experiments (*13*). A typical experiment involves TOF analysis of the products emitted at some angle with respect to a laboratory fixed direction (often this direction is chosen to be the direction of the reactant atom beam). The detector position can be rotated so that data can be collected at several angles. At each angle, only a small portion (typically 10^{-4}) of the products is detected, which results in long hours of signal averaging. Subsequently, normalization of the data to a fixed angle and transformation of the data from the laboratory frame to the center-of-mass frame is necessary to obtain the DCS. In spite of the experimental challenges, state-resolved DCS measurements for D + H_2 have been reported by Buntin *et al.* (*14*) for a few angles at collision energies of 0.8 and 1.20 eV and by Continetti *et al.* (*15*) for a wide distribution of angles at collision energies of 0.53 and 1.01 eV. In both experiments TOF analysis of the HD product was sufficient to resolve individual vibrational but not individual HD rotational states. In an alternative approach, Schnieder *et al.* (*16*) have used Rydberg atom TOF translational spectroscopy to measure the vibrationally resolved DCS for the H + D_2 reaction at collision energies of 0.54 and

T. N. Kitsopoulos and D. W. Chandler are in the Combustion Research Facility, Sandia National Laboratories, Livermore, CA 94551. M. A. Buntine is in the Department of Chemistry, Yale University, New Haven, CT 06511. D. P. Baldwin is in the Ames Laboratory, Iowa State University, Ames, IA 50011. R. N. Zare is in the Department of Chemistry, Stanford University, Stanford, CA 94305.

*To whom correspondence should be addressed.

1.29 eV. More recently, by reducing the energy spread in their D_2 beam, Schnieder and Welge (*17*) have reported the first rotationally resolved DCS measurement for this fundamental reaction.

As an evolutionary step toward the present reaction product imaging (RPI) experiments, Buntine *et al.* (*18*) studied the H + HI → $H_2(v = 1, J = 11,13$, where v is the vibrational quantum number and J is the rotational quantum number) + $I(^2P_{3/2,1/2})$ reaction at collision energies of 1.7 and 2.6 eV with the ion-imaging technique. In this experiment, carried out in a single molecular beam, it was possible to measure branching ratios for the various reaction channels that were observed; however, measurement of the DCS was prohibited because of the lack of a defined initial velocity for the reactants. More recently, Houston and co-workers (*19*) used a crossed–molecular beam ion-imaging technique to successfully measure the state-resolved DCS for the inelastic scattering of NO from Ar. The approach was similar in practice to the experiment presented here and arose from collaborative work using ion-imaging techniques to study unimolecular dissociation processes (*3*).

Experimental Apparatus

A schematic of the experimental apparatus used in this study is shown in Fig. 1. The apparatus is a modified version of the single-beam, ion-imaging photofragment spectrometer described in detail elsewhere (*20*). In brief, a photolytically produced beam of H atoms is crossed with a supersonic molecular beam of D_2 molecules. Product D atoms are ionized and accelerated toward a position-sensitive ion detector consisting of microchannel plates coupled to a phosphor screen. An image is created on the phosphor, which is the 2-D projection of the 3-D distribution of the D atom products. The image is recorded and averaged with a charged-coupled-device (CCD) camera.

A 30% mixture of HI/He (backing pressure, 20 psi) and pure D_2 (backing pressure, 55 psi) is expanded supersonically into the source vacuum chamber through a pair of parallel solenoid valves (General Valve series 9). Both gas expansions are skimmed 1.0 cm from the nozzle orifices and collimated to diameters of 3 mm by means of a pair of collimating holes in the repeller plate. In this manner a pair of parallel molecular beams are produced in the reaction chamber, 2 cm apart, at a distance of 7 cm from the nozzle orifices. The beam of H atoms is produced by photolyzing HI midway through the extraction field (see Fig. 1) using the fourth harmonic (266 nm) of a Nd:yttrium-aluminum-garnet (YAG) laser operating at 30 Hz (Spectra Physics GCR-3, 8 to 10 mJ per pulse). To match the diameter of the molecular beam, the laser beam is focused to 3 mm with a lens that has a focal length of 1.0 m. We find that these conditions produce the maximum flux of H atoms at the D_2 beam.

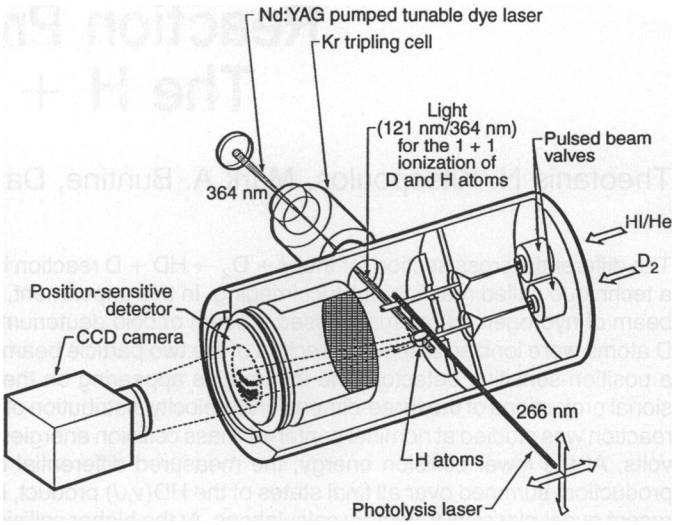

Fig. 1. Schematic of the reaction product imaging apparatus. A photolytically produced beam of H atoms is crossed with a supersonic molecular beam of D_2 molecules. Product D atoms are ionized and accelerated toward a position-sensitive ion detector consisting of microchannel plates coupled to a phosphor screen. Ion positions appearing on the phosphor screen are recorded with a CCD camera.

The multiphoton ionization of the product D atoms is accomplished by absorption of a vacuum ultraviolet (VUV, 121.6 nm, Lyman-α wavelength) and UV (364.8 nm) photon. The VUV photon resonantly excites the D(1*s*) atom to the 2*p* state. Subsequent absorption of the UV photon either ionizes the D atom directly or excites it to a very high Rydberg level, at which it then field ionizes because of the presence of the extraction field (*15*). The UV light is generated by frequency doubling of the output of a Nd:YAG pumped dye laser system (Spectra Physics GCR-5, and PDL-1, respectively). The VUV Lyman-α light is generated by frequency tripling of the UV light in a Kr/Ar gas mixture (total pressure 550 torr) adjusted to achieve optimum phase matching (*21*). A lens with a focal length of 20 cm is used to focus the 364.8-nm light in a cell containing the Kr/Ar mixture. The VUV and the residual UV laser light pass through an LiF lens and onto the point where the H atom beam crosses the D_2 molecular beam. The spot size of the VUV laser light at the position of the D_2 molecular beam is about 3 mm. Matching the diameter size of the VUV ionization laser beam to the diameter size of the D_2 beam (3 mm) and the width of the H atom beam (3 mm) ensures that all velocity components of the D atom products interact with the ionization laser for the same amount of time (5 ns) and thus are ionized with equal efficiency. Both the frequency and the intensity of the generated Lyman-α photons are optimized by monitoring the resonant ionization yield of background D or H atoms produced by the thermal decomposition of D_2 or H_2 on the hot filament of an ionization gauge. It is imperative that during data acquisition all ion gauges are turned off; otherwise, the thermal D atoms produced in this fashion will dominate the observed image.

The propagation direction of the ionization laser beam is perpendicular to the plane formed by the two crossed beams. Consequently, the 1*s*-2*p* transition of the D atoms scattering out of this plane experiences a Doppler shift (*22*), that is, a shift in the resonant frequency needed to excite and subsequently ionize them (a blue shift for those proceeding away from the laser propagation direction and a red shift for those proceeding toward the laser propagation direction). For the collision energies studied in this experiment, we estimate the maximum Doppler shift to be approximately 3 to 4 cm^{-1}. The bandwidth of our VUV laser light is about 1.5 cm^{-1}; therefore, to ensure that all velocity components are equally detected, we scan the frequency of the VUV laser over the transition as the image is recorded. A typical scan covers a 15-cm^{-1} range.

An important parameter in this study is the population of rotational states of the D_2 molecule in the molecular beam. To determine the rotational populations, we use 2 + 1 REMPI (*23*) of $D_2(v'' = 0, J'')$ through the $v' = 0$ level of the E,F state, and measure the D_2^+ ion yield for each $D_2(v'' = 0, J'')$ state. By comparing the relative D_2^+ signal levels from the different rovibronic transitions with those obtained by the same technique on room-temperature D_2, we determined that the relative rotational populations in the D_2 are 1.0, 0.5, and 0.5 for $J'' = 0$, 1, and 2, respectively.

Results of the RPI Measurements

Two product channels are open when HI is photodissociated with 266-nm photons; these correspond to formation of iodine in

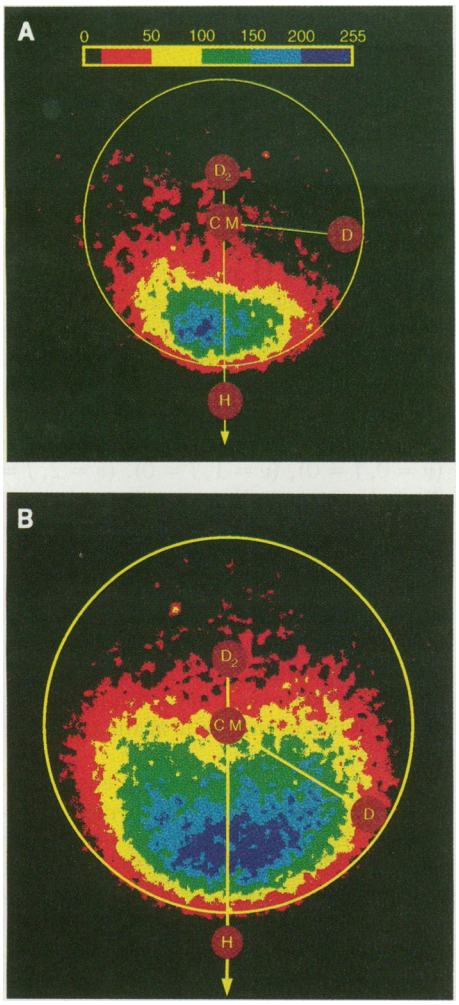

Fig. 2. Data images for the product D atoms produced from the reaction H + D_2 → HD + D at nominal center-of-mass collision energies of (**A**) 0.54 eV and (**B**) 1.29 eV. The image intensities are scaled between 0 and 255, and the intensity scale of the image color map is indicated in the figure. The open circles represent the calculated position of scattered D atoms corresponding to HD(v = 0, J = 0). The direction of the H atom beam is indicated by the arrow, and the positions of the D_2 beam and the center of mass of the reaction are indicated by the solid circles labeled D_2 and CM, respectively.

the $^2P_{3/2}$ ground state and in the $^2P_{1/2}$ excited spin-orbit state:

$$HI + 266\ nm \rightarrow H + I(^2P_{3/2}),$$

$$K.E._H^{lab} = 1.59\ eV\ (fast\ channel)$$

$$HI + 266\ nm \rightarrow H + I(^2P_{1/2}),$$

and

$$K.E._H^{lab} = 0.66\ eV\ (slow\ channel)$$

where $K.E._H^{lab}$ is the kinetic energy of the hydrogen in the laboratory frame of reference. In the center-of-mass frame, the collision energies for reaction of H atoms with D_2 that correspond to these two channels are E_{CM} = 1.29 and 0.54 eV, respectively. As

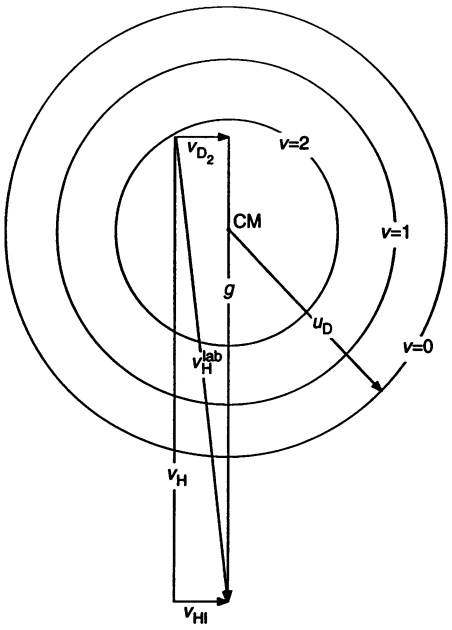

Fig. 3. Newton diagram for the reaction H + D_2 → HD(v = 0, 1, 2; J = 0) + D at nominal center-of-mass collision energy of 1.29 eV. The vectors $\mathbf{v}_{HI}$ and $\mathbf{v}_{D_2}$ represent the HI and D_2 beam velocities, respectively ($\mathbf{v}_{HI} \approx \mathbf{v}_{D_2}$); $\mathbf{v}_H$ is the H atom velocity obtained from the HI dissociation; $\mathbf{v}_H^{lab}$ is the velocity of the H atoms in the laboratory frame ($\mathbf{v}_H^{lab} = \mathbf{v}_H + \mathbf{v}_{HI}$); $\mathbf{g}$ is the relative velocity of the collision ($\mathbf{v}_H \approx \mathbf{g}$); $\mathbf{u}_D$ is the D atom velocity in the center-of-mass frame; CM represents the position of the center of mass of the system, and the circles indicate the calculated D atom Newton circles corresponding to formation of HD(v = 0, 1, 2; J = 0) product states.

reported elsewhere (*24*), the angular distribution of the H atoms for the two channels is strongly coupled to the polarization of the dissociation laser. The transition associated with dissociation into the slow channel is a parallel one and leads to a $\cos^2\theta$ distribution (θ is the scattering angle) of H atoms (H atoms preferentially moving along the laser polarization axis with a node in the distribution perpendicular to the axis). For the fast channel, H atoms are produced by excitation through a perpendicular transition leading to a $\sin^2\theta$ distribution (H atoms preferentially traveling perpendicular to the laser polarization axis with a node in the distribution along the laser polarization axis). This separation of the two H atom channels allows us to choose cleanly the velocity of the reactant H atoms by simply choosing the polarization direction of the linearly polarized light (266 nm) that photolyzes the HI molecular beam.

Product Images

Reaction product images of the D atoms produced from the H + D_2 reaction, at collision energies of 0.54 and 1.29 eV, are shown in Fig. 2, A and B, respectively. The orientation of both images is such that the H atom beam lies in the plane of the image and is directed from the top of the image toward the bottom; the D_2 beam is directed out of the plane toward the viewer. Both images are obtained by averaging 180,000 laser shots and subtracting a background image. Background images are obtained by adjusting the time delay of the HI photolysis laser such that the H atoms and the D_2 beam do not intersect during the VUV laser pulse. Typical D^+ count rates for this experiment are 0.3 to 1.0 ion per laser shot. Superimposed on the data images of Fig. 2 are circles representing the maximum speed that the D atoms can attain from the reaction under the assumption that the HD product is formed in its ground vibrational and rotational state (v = 0 and J = 0).

The velocity vector (Newton) diagram relevant to our experiment is shown in Fig. 3. Newton diagrams are used to transform product velocities measured in the laboratory frame into center-of-mass velocities. For bimolecular scattering, the angular distribution of the products is cylindrically symmetric with respect to the relative velocity (g) of the reactants. Consequently, an inverse Abel transform (*20*, *25*) can be used to reconstruct the 3-D velocity distribution when g is oriented parallel to the image plane (the face of the detector). In our experimental setup we make the HI velocity comparable to that of the D_2 beam ($\mathbf{v}_{HI} \approx \mathbf{v}_{D_2}$) by seeding the HI beam in He. Hence, in the laboratory reference frame, $\mathbf{g} \approx \mathbf{v}_H$ (see Fig. 3), where $\mathbf{v}_H$ is the H atom velocity obtained from the HI dissociation. The direction of $\mathbf{v}_H$ is defined by the crossing point of the 266-nm photolysis laser beam with the HI beam and the crossing point of the VUV ionization laser beam with the D_2 beam. This direction is maintained parallel to our position-sensitive detector (that is, the imaging plane) during the experiments.

In the data images of Fig. 2, structural details representing individual HD rovibrational states are not observed for several reasons. First, our ion images represent by their nature a 2-D projection of a 3-D velocity distribution. In three dimensions, scattered D atoms corresponding to a specific HD(v,J) lie on a sphere (known as a scattering surface, or a Newton sphere), whose radius is proportional to their recoil speed. Consequently, for an ensemble of HD final states, each having its own scattering surface, the D atom velocity distribution will be represented by a series of concentric spheres. If the product angular distribution on each scattering surface is similar, then the projections of these spheres onto the image plane would overlap (that is, the spheres would be crushed on

top of each other). Thus, the intensity of each point in the data image would in general have contributions from several HD product states; as a result, observable structure would be expected to be diminished.

A second reason why individual rings are not observed in the data images is because we have "geometric smearing," which is a direct consequence of the finite dimensions of the reaction volume. The size of our reaction volume [about $(0.3\ cm)^3$], defined by the overlap of the H atom beam, the D_2 beam, and the ionization laser beam, is sufficiently large to cause the Newton sphere of the D atoms associated with neighboring HD quantum states to overlap. In the extreme limit, where the particle beams and laser beam would be sufficiently small, such that the products emanated from a point-like source, individual quantum states of the HD product would be observed. Geometric smearing in RPI is not insurmountable and can be "remedied" by proper data analysis in situations where the nature of the smearing is well defined (image restoration) (*26, 27*). Because the exact nature of the blurring in the present experiment has not been independently measured (that is, we have not measured a known distribution and therefore experimentally determined our blurring), we cannot deconvolve the data for the particle beam sizes and the laser ionization volume.

Reconstructed Product Images

The 2-D intensity profile through the 3-D velocity distributions for the D atoms, obtained from the data through an inverse Abel transform (*20, 27*), is shown in Fig. 4, A and B, for the two collision energies of 0.54 and 1.29 eV, respectively. We refer to these as the reconstructed images; these images should not be confused with the data images of Fig. 2, which are 2-D projections of the 3-D velocity distribution. The 3-D velocity distribution of the D atoms can be generated by rotating the reconstructed images about their symmetry axis, in this case the direction of the relative velocity **g**. To draw the analogy to the more conventional crossed-beam TOF scattering experiments, these images are equivalent to velocity contour plots of the scattering process. The "noisiness" down the centers of both images in Fig. 4 is introduced by the reconstruction algorithm. To reduce some of the noise caused by the inverse Abel transformation, we "smoothed" the data images beforehand by fitting a Gaussian (5 pixels in half-width) to every 9 sequential image pixels. The extent of the "smoothing" Gaussian is smaller than the resolution of the present experiment (about 17 pixels), thus ensuring that any structure present in the data has not been lost by this smoothing procedure. The data images shown in Fig. 2 have not been smoothed. Overlaid on the images are several Newton circles, indicating the calculated positions of scattered D atoms, corresponding to HD(v,J) product states.

Although we are unable to resolve individual quantum states of the HD product in the reconstructed images of the D atoms, both qualitative and quantitative information pertaining to the reaction can be extracted from the images. On a qualitative level, inspection of Fig. 4A (E_{CM} = 0.54 eV) reveals that the D atoms are strongly peaked along the beam direction of the H atoms and that their distribution is relatively narrow [there is not much intensity at velocities that would correspond to HD(v = 1) being formed]. This observation supports the theoretical predictions (*4, 8–11*) that at low collision energies HD will be formed predominantly in v = 0 and in low rotational states and product D atoms will be forward scattered with respect to the direction of the H atom beam velocity.

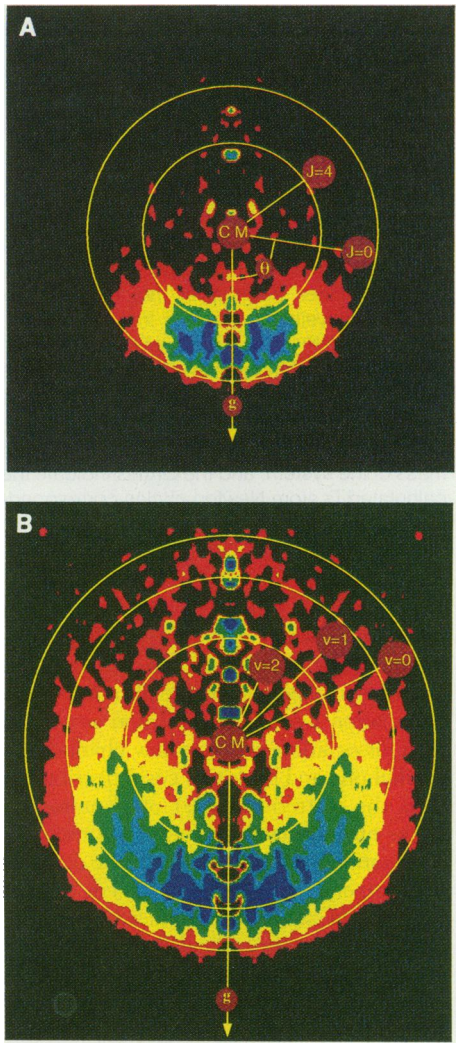

Fig. 4. Reconstructed images for the product D atoms produced from the reaction H + D_2 → HD + D at nominal center-of-mass collision energies of (**A**) 0.54 eV and (**B**) 1.29 eV. The image intensity is scaled between 0 and 255, and the image color map is identical to that used in Fig. 2. The open circles represent the calculated positions of scattered D atoms corresponding to HD(v = 0, J = 0) and HD(v = 0, J = 4) in (A) and HD(v = 0, J = 0), HD(v = 1, J = 0) and HD(v = 2, J = 0) in (B). The position of the center of mass for the reaction is indicated by the solid circle labeled CM, and the direction of the relative velocity by the vector **g**.

Inspection of the reconstructed ion image of Fig. 4B (E_{CM} = 1.29 eV) reveals information not readily observed in the corresponding data image of Fig. 2B. With the visual aid offered by the overlaid Newton circles for selected HD quantum states (v = 0, J = 0), (v = 1, J = 0), (v = 2, J = 0), it is apparent that at wider scattering angles formation of internally excited HD is the dominant channel of the reaction. Although very wide angle scattering is observed, there is no evidence of direct D atom backscattering (D atoms moving against the direction of the incoming H atoms), which would imply the formation of a long-lived complex near the transition state (*28*).

Accurate ab initio potential energy surfaces are available for the hydrogen exchange reaction (*5, 29, 30*). Although DCSs for H + H_2(HD) and D + H_2 have been calculated with the use of fully converged 3-D quantum scattering calculations (*12*), researchers who have carried out similar calculations on the H + D_2 reaction have reported only on the integral cross sections (*11*). Recently, however, Aoiz *et al.* (*4*) have simulated the state-to-state DCSs for the latter reaction with a QCT calculation based on the LSTH (*5*) potential energy surface. At the collision energies studied, 0.54 and 1.29 eV, and for the D_2(v'' = 0, J'' = 0,1,2) initially populated, the calculation predicts that the D atom product is predominantly forward scattered, which is in qualitative agreement with our experimental observations.

Comparison with QCT Calculations

To compare quantitatively our experimental angular distributions to those predicted by the QCT simulation, we have plotted in Fig. 5, A and B, the total D atom yield from the reaction as a function of scattering angle θ, where θ is defined with respect to the direction of the relative velocity vector **g** (Fig. 4A). We have integrated the intensity of our reconstructed images along radial slices, centered at the center of mass of the reaction. Each radial slice is a 4° sector whose radius is equal to the radius of the largest Newton circle [that is, the one corresponding to formation of HD(v = J = 0)]. For E_{CM} = 0.54 eV (Fig. 5A), the agreement between theory and experiment

is very good for $\theta > 10°$, but the theory overestimates the intensity relative to the experiment at small scattering angles. This difference could be caused by the fact that the inverse Abel transformation introduces some intensity errors in the reconstructed image near the symmetry axis (*27*). This may be a consequence of the nature of the reconstruction process, which works from the outside of the image toward the center. Propagation of the error during this process means that the relative error is largest at the symmetry axis.

For the higher collision energy, 1.29 eV, it is clear from Fig. 5B that the agreement between the QCT calculation and the experiment is not as good as for the E_{CM} = 0.54 eV case. Qualitatively, a slight inflection in the DCS slope at about 45° is observed in both the theoretical and experimental results. Quantitatively, at small scattering angles the observed DCS is larger then the QCT prediction, but at higher scattering angles this trend is reversed. One possible experimental explanation for this deviation could be that our data are not normalized to the power of the VUV ionization laser. The VUV generation is optimized by monitoring D^+ yield from thermal D atoms, which corresponds to optimizing the center of the Doppler profile for the D atom products. Because the optimum Kr/Ar pressures for maximum VUV generation vary with wavelength, it is possible that the ionization laser power is not constant over the entire product D atom Doppler profile that is scanned to obtain complete ion images. To study this effect, we added acetone to the D_2 beam and monitored the $[acetone]^+$ yield from the absorption of the VUV laser light (one-photon ionization) and observed only a 10% variation over the spectral range of the D atom Doppler profile. This intensity variation is too small to make up for the observed discrepancy between the QCT predictions and the experimental results.

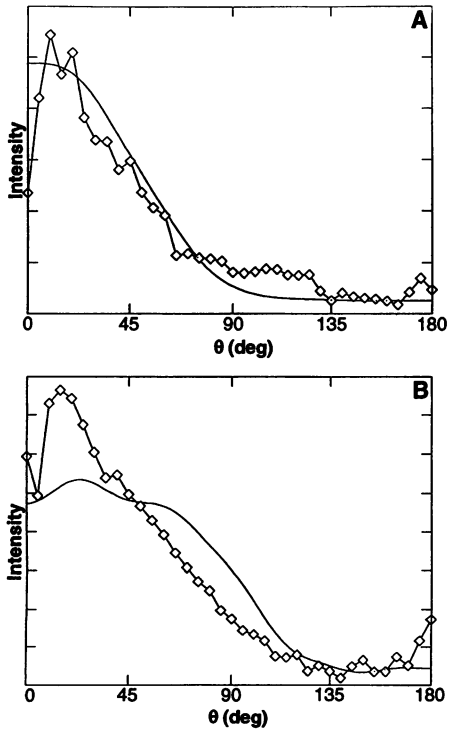

Fig. 5. The DCS for D atom production from the reaction $H + D_2 \rightarrow HD + D$ at nominal center-of-mass collision energies of (**A**) 0.54 eV and (**B**) 1.29 eV, summed over all final states of the HD(*v*,*J*) product; θ is the center-of-mass scattering angle; (◇) this experiment; (solid line) the results of the QCT calculation of Aoiz *et al.* (*4*).

We can also compare our results to the DCS measurements obtained by crossed-beam TOF experiments for the hydrogen exchange reactions. Schnieder *et al.* (*16*) have measured the angular distribution of D atoms from the $H + D_2 \rightarrow HD + D$ reaction. They found that at a collision energy of 0.54 eV the reaction produces HD($v = 0$, low *J*) and is backscattered with respect to the H atom beam direction. At a collision energy of 1.29 eV, they observed that the scattering angle for the D atoms increases with increasing vibrational and rotational excitation of the HD product. Although these observations are qualitatively similar to our results, because the center-of-mass DCS was not reported in the study of Schnieder *et al.*, quantitative comparison between the two studies is not possible. The most detailed experimental measurement concerning the DCS for the hydrogen exchange reaction has been made by Continetti *et al.* (*15*) for the $D + H_2 \rightarrow HD + H$. Their results show that, at a collision energy of 0.51 eV, the reaction produces HD($v = 0$) in low rotational states and is scattered backward (180°) with respect to the D atom beam velocity, whereas, at the higher collision energy (0.98 eV), the DCS for the HD product peaks at a smaller angle (125°). The results compared well with the quantum mechanical trajectory calculations (*12*) based on the LSTH surface. It is interesting that the experimental DCS of Continetti *et al.* (*15*) also showed an increased amount of HD backscattering when compared to the theory, as do our results.

Conclusions

We have applied an ion-imaging technique, RPI, to the study of bimolecular reactive scattering, which we believe will be a powerful method for studying reaction dynamics. RPI offers several advantages over traditional methods: (i) The 4π particle collection efficiency leads to count rates that are capable of producing product angular distributions for the reaction within a few hours; (ii) the technique samples the entire product angular distribution simultaneously; and (iii) a single quantum state of the product, in this case ground-state D atoms, can be selected by utilizing REMPI. Also, instead of imaging the atomic fragment, the molecular product can be ionized in a quantum state–selective manner and its ion image recorded. This will yield the DCS for a single rovibrational quantum state of the molecular product, a measurement that will allow a most stringent test of theory.

In the present experimental study on the $H + D_2 \rightarrow HD + D$ reaction, our experimental results are in fair agreement with a QCT calculation based on the LSTH potential energy surface. Although we have suggested some experimental reasons for the differences observed between theoretical predictions and the experimental results, this does not eliminate the possibility that improvements in the theoretical treatment might be necessary to bridge the disagreement.

REFERENCES AND NOTES

1. F. London, *Z. Elektrochem.* **35**, 552 (1929).
2. H. Eyring and M. Polanyi, *Z. Phys. Chem. Abt. B* **12**, 279 (1931).
3. D. W. Chandler and P. L. Houston, *J. Chem. Phys.* **87**, 1445 (1987).
4. F. J. Aoiz, V. J. Herrero, O. Puentedura, V. Sáez Rábanos, *Chem. Phys. Lett.* **198**, 321 (1992).
5. B. Liu, *J. Chem. Phys.* **58**, 1925 (1973); P. Siegbahn and B. Liu, *ibid.* **68**, 2457 (1978); D. G. Truhlar and C. J. Horowitz, *ibid.*, p. 2466.
6. K. D. Rinnen, D. A. V. Kliner, R. S. Blake, R. N. Zare, *Chem. Phys. Lett.* **153**, 371 (1988); K. D. Rinnen, D. A. V. Kliner, R. N. Zare, *J. Chem. Phys.* **91**, 7514 (1989); D. A. V. Kliner, K. D. Rinnen, R. N. Zare, *Chem. Phys. Lett.* **166**, 107 (1990); D. A. V. Kliner and R. N. Zare, *J. Chem. Phys.* **92**, 2107 (1990); D. A. V. Kliner, D. E. Adelman, R. N. Zare, *ibid.* **94**, 1069 (1991); *ibid.* **95**, 1648 (1991); D. Neuhauser *et al.*, *Science* **257**, 519 (1992).
7. D. L. Phillips, H. B. Levene, J. J. Valentini, *J. Chem. Phys.* **90**, 1600 (1989); J. C. Nieh and J. J. Valentini, *ibid.* **92**, 1083 (1990).
8. N. C. Blais and D. G. Truhlar, *Chem. Phys. Lett.* **162**, 503 (1989); N. C. Blais *et al.*, *J. Chem. Phys.* **91**, 1038 (1989); M. Zhao and D. G. Truhlar, *J. Phys. Chem.* **94**, 6696 (1990).
9. W. J. Keogh *et al.*, *Chem. Phys. Lett.* **195**, 144 (1992).
10. F. J. Aoiz, V. J. Herrero, O. Puentedura, V. Sáez Rábanos, *ibid.* **169**, 243 (1990); F. J. Aoiz, V. J. Herrero, V. Sáez Rábanos, *J. Chem. Phys.* **97**, 7423 (1992).
11. D. E. Manolopoulos and R. E. Wyatt, *Chem. Phys. Lett.* **159**, 123 (1989); M. D'Mello, D. E. Manolopoulos, R. E. Wyatt, *J. Chem. Phys.* **94**, 5985 (1991).
12. J. Z. H. Zhang and W. H. Miller, *Chem. Phys. Lett.* **153**, 465 (1988); *ibid.* **159**, 130 (1989); *J. Chem. Phys.* **91**, 1528 (1989).
13. R. Goetting, H. R. Mayne, J. P. Toennies, *J. Chem. Phys.* **80**, 2230 (1984); *ibid.* **85**, 6396 (1986).
14. S. A. Buntin, C. F. Giese, W. R. Gentry, *ibid.* **87**, 1443 (1987); *Chem. Phys. Lett.* **168**, 513 (1990).
15. R. E. Continetti, B. A. Balko, Y. T. Lee, *J. Chem. Phys.* **93**, 5719 (1990).
16. L. Schnieder, K. Seekamp-Rahn, F. Liedeker, H. Steuwe, K. H. Welge, *Faraday Discuss. Chem. Soc.* **91**, 259 (1991).
17. L. Schnieder and K. H. Welge, XIVth International Symposium on Molecular Beams, Abstracts of invited talks and contributed papers, Asilomar, CA, 7 to 12 June 1992 (organized by G. Scoles *et al.*), p. 27.

18. M. A. Buntine, D. P. Baldwin, R. N. Zare, D. W. Chandler, *J. Chem. Phys.* **94**, 4672 (1991).
19. A. L. Suits, L. S. Bontuyan, P. L. Houston, B. J. Whitaker, *ibid.* **96**, 8618 (1992).
20. D. W. Chandler, J. W. Thoman, Jr., M. H. M. Janssen, D. H. Parker, *Chem. Phys. Lett.* **156**, 15 (1989); D. P. Baldwin, M. A. Buntine, D. W. Chandler, *J. Chem. Phys.* **93**, 6578 (1990); W. P. Hess, D. W. Chandler, J. W. Thoman, Jr., *Chem. Phys.* **163**, 277 (1992).
21. R. Wallenstein, *Opt. Commun.* **33**, 119 (1980); R. Hilbig and R. Wallenstein, *IEEE J. Quantum Electron.* **QE-17**, 1566 (1981); *ibid.* **QE-19**, 194 (1983).
22. W. Demtröder, *Laser Spectroscopy* (Springer-Verlag, New York, 1982), p. 86.
23. E. E. Marinero, C. T. Rettner, R. N. Zare, *Phys. Rev. Lett.* **48**, 1323 (1982); E. E. Merinero, R. Vasudev, R. N. Zare, *J. Chem. Phys.* **78**, 692 (1983); K. D. Rinnen, M. A. Buntine, D. A. V. Kliner, R. N. Zare, *ibid.* **95**, 214 (1991); W. M. Huo, K. D. Rinnen, R. N. Zare, *ibid.*, p. 205; D. E. Adelman, N. E. Shafer, D. A. V. Kliner, R. N. Zare, *ibid.* **97**, 7323 (1992).
24. R. D. Clear, S. J. Riley, K. R. Wilson, *J. Chem. Phys.* **63**, 1340 (1975); R. Schmiedl, H. Dugan, W. Meier, K. H. Welge, *Z. Phys. A* **304**, 137 (1982).
25. R. N. Bracewell, *The Fourier Transform and Its Applications* (McGraw-Hill, New York, 1986).
26. G. C. Gonzalez and P. Wintz, *Digital Image Processing* (Addison-Wesley, London, 1977).
27. R. N. Strickland and D. W. Chandler, *Appl. Opt.* **30**, 1811 (1991).
28. W. H. Miller and J. Z. H. Zhang, *J. Phys. Chem.* **95**, 12 (1991).
29. A. J. Varandas, F. B. Brown, C. A. Mead, D. G. Truhlar, N. C. Blais, *J. Chem. Phys.* **86**, 6258 (1987).
30. A. I. Boothroyd, W. J. Keogh, P. G. Martin, M. R. Peterson, *ibid.* **95**, 4343 (1991).
31. We thank M. J. Jaska for technical support, and F. J. Aoiz for providing the QCT results for the H + D_2 reaction. T.N.K. thanks R. E. Continetti for many enlightening discussions. M.A.B. and R.N.Z. acknowledge support from the National Science Foundation (under grant CHE 90-7939). This work is supported by the U.S. Department of Energy, Office of Basic Energy Sciences, Division of Chemical Sciences.

The Biological and Social Phenomenon of Lyme Disease

Alan G. Barbour and Durland Fish

Lyme disease, unknown in the United States two decades ago, is now the most common arthropod-borne disease in the country and has caused considerable morbidity in several suburban and rural areas. The emergence of this disease is in part the consequence of the reforestation of the northeastern United States and the rise in deer populations. Unfortunately, an accurate estimation of its importance to human and animal health has not been made because of difficulties in diagnosis and inadequate surveillance activities. Strategies for prevention of Lyme disease include vector control and vaccines.

Lyme disease is a zoonosis, an inadvertent infection of humans with an animal pathogen. In temperate regions of the Northern Hemisphere, ticks transmit the etiologic bacterium *Borrelia burgdorferi* from its usual wildlife reservoirs to humans and domestic animals (*1*, *2*). In the United States, Lyme disease occurs primarily in suburban and rural areas (*3*). Early infection of humans is usually a self-limited, flu-like illness with a skin rash where the tick imbeds itself (*4*) (Fig. 1). After a few weeks to several months, as many as 70% of untreated, infected patients suffer the effects of bacterial invasion of one or more distant organs or systems, including the brain, nerves, eyes, joints, and heart (*5*). These late manifestations, particularly the dysfunction of the central nervous system and chronic arthritis, are disabling but rarely fatal (*5*).

In the United States during 1991, 9465 cases of Lyme disease were formally reported, making it by far the most common arthropod-borne disease (*6*). The rising incidence and geographic spread of this zoonosis have interested the general public (*7*). Lyme disease probably ranks only behind acquired immunodeficiency syndrome in media coverage of infectious diseases in the United States over the last decade. News, public health programs, and patient advocacy groups have informed the public of the symptoms of Lyme disease and of ways to avoid infection (*8*). A less salubrious consequence of the attention has been the attribution to *B. burgdorferi* of a number of ills, only a fraction of which are likely to be Lyme disease (*9*, *10*). Wisconsin had 545 reported cases of Lyme disease in 1989; in the same year, 94,000 serum samples were received by reference laboratories in the state for Lyme disease testing (*11*). Georgia reported hundreds of cases of Lyme disease until it was documented that there were few ticks bearing *B. burgdorferi* in the state (*12*).

A provisional diagnosis of Lyme disease is often acceptable to patients with vexing, undefined illnesses, not only because there is hope for a cure with antibiotics but also because Lyme disease is acquired through what are generally perceived to be wholesome activities, such as hiking and working out-of-doors (*7*). The full extent to which people are being inappropriately treated with antibiotics cannot be estimated at present, but it is likely that a large minority, if not a majority, of the health care dollars expended on therapy for Lyme disease are for inaccurate diagnoses of *B. burgdorferi* infection (*9*, *10*). Some of these resources would better benefit the community if directed toward methods of disease prevention, such as vector control. A zoonosis can be characterized with respect to the microbiology of the agent, the ecology in relation to vectors and reservoir hosts, and the epidemiology of human disease. Full description of the phenomenon of Lyme disease will also require consideration of behavioral and economic factors in the response to the disease's emergence. These social factors are still poorly understood.

A. G. Barbour is in the Departments of Microbiology and Medicine, University of Texas Health Science Center, San Antonio, TX 78284. D. Fish is in the Medical Entomology Laboratory, Department of Community and Preventive Medicine, New York Medical College, Valhalla, NY 10595.

The Origins of Lyme Disease in North America

The clinical syndrome of *B. burgdorferi* infection had been described in Europe (*13*) more than six decades before Steere and colleagues in 1975 investigated an unusual cluster of childhood arthritis in the coastal community of Lyme, Connecticut (*14*). Soon after the Connecticut investigation, the relation between the arthritis and a prior episode of the characteristic skin rash, erythema migrans (Fig. 1), common in Europe, was noted (*15*). The search for an etiologic agent implicated a tick, *Ixodes scapularis* (*I. dammini*), as the vector on epidemiological grounds (*16*). The bite of a related species, *I. ricinus*, was known to cause erythema migrans in Europe (*17*). Identity between the two tick-borne conditions was established when *B. burgdorferi* was first isolated from *I. scapularis* and *I. ricinus* and then from patients in the United States and Europe with Lyme disease and erythema migrans (*18*).

The events leading to an epidemic of arthritis in residents of Lyme began several centuries earlier. Infections from *B. burgdorferi* probably occurred in North America before the first waves of European colonization. Erythema migrans, the hallmark of *B. burgdorferi* infection, was already present in midwestern and Pacific states at the time Lyme disease was first described in Connecticut (*19*). Early descriptions of colonial forests, the abundance of deer, and ticks annoying explorers suggest that the condi-